



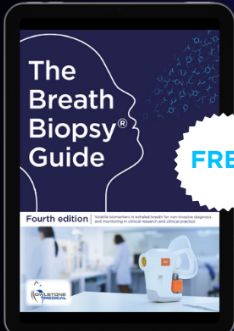
## Relative and absolute intensity calibrations of a modern broadband echelle spectrometer

To cite this article: N Bibinov *et al* 2007 *Meas. Sci. Technol.* **18** 1327

View the [article online](#) for updates and enhancements.

### You may also like

- [The influence of spectral calibration error of the hyperspectral remote sensor on the TOA radiance](#)  
Yaqiong Zhang, Wenjuan Zhang and Zhengchao Chen
- [Fast TPC Online Tracking on GPUs and Asynchronous Data Processing in the ALICE HLT to facilitate Online Calibration](#)  
David Rohr, Sergey Gorbunov, Mikolaj Krzewicki et al.
- [Decision Making of Telecommunication Device Calibration Rates](#)  
Gayuh Raditya Prabandanu and Zulfa Fitri Ikatrinasari



**FREE** **The Breath Biopsy® Guide**  
Fourth edition

[DOWNLOAD THE FREE E-BOOK](#)

BREATH BIOPSY®



# Relative and absolute intensity calibrations of a modern broadband echelle spectrometer

N Bibinov, H Halfmann, P Awakowicz and K Wiesemann

Ruhr-Universität Bochum, Allgemeine Elektrotechnik und Plasmatechnik, D-44780 Bochum, Germany

Received 13 July 2006, in final form 29 December 2006

Published 13 March 2007

Online at [stacks.iop.org/MST/18/1327](http://stacks.iop.org/MST/18/1327)

## Abstract

We report on relative and absolute intensity calibrations of a modern broadband echelle spectrometer (type ESA 3000<sup>®</sup> trademark of LLA Instruments GmbH, Berlin) for use in the diagnostics of low-temperature plasma. This type of device measures simultaneously complete emission spectra in the spectral range from 200 to 800 nm with a spectral resolution of several picometres by using more than 90 spectral orders, causing a strongly structured efficiency function. The assumptions and approximations entering the calibration procedure under these conditions are discussed in section 3. For coping with the strongly structured efficiency function a continuum light source is needed, which covers the entire spectral range. Furthermore, the variation of its intensity must be low enough to ensure that neither statistical errors perturb the calibration in regions with low photon flux and/or low efficiency, nor local memory overflow in regions with high photon flux or high efficiency. In our case this requires that during calibration over the whole spectral range of the spectrometer the counts per pixel in one measurement vary at highest by a factor 10 to 12. Usual broadband light sources do not meet this latter requirement. We, therefore, use an uncalibrated ‘composite’ source, an adjustable combination of a standard tungsten strip lamp and a deuterium lamp, and calibrate the spectrometer in a two-step process against the tungsten strip lamp and well-known rovibrational intensity distributions in the emission spectra of NO and N<sub>2</sub>. We adjust the composite source in a way to produce a perturbation-free first approximation of an (uncalibrated) efficiency function, which is then corrected and thus calibrated by comparison with the (secondary) standards mentioned above. For absolute calibration we use the tungsten strip lamp. The uncertainty attained in this way for the relative calibration depends on the wavelength and varies between 5% and 10%. For the absolute calibration we obtained an uncertainty of 12%. We further discuss problems caused by the non-uniform spectral efficiency and dispersion of the spectrometer, which complicate the calibration procedure.

**Keywords:** echelle spectrometer, relative intensity calibration, absolute intensity calibration

## 1. Introduction

In contrast to classical echelle spectrometers, which display in one or two spectral orders a spectral region, preselected

by a monochromator, modern broadband echelle spectrometer combine high resolution with the possibility of simultaneously measuring spectra over a broad spectral range, typically from 200 to 800 nm. This makes them apt for diagnostics

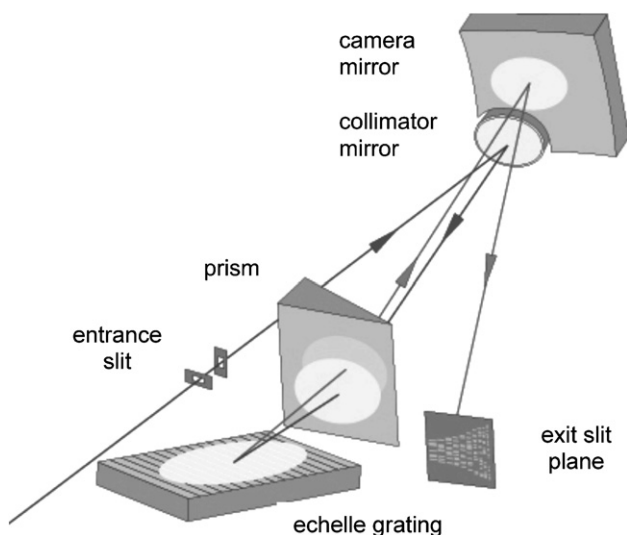


**Figure 1.** Scheme of the broadband echelle spectrometer ESA 3000<sup>®</sup> (trademark of LLA Instruments GmbH Berlin, figure reprinted with permission of K Lobe, LLA Instruments GmbH).

of low temperature plasmas, especially those running in molecular gases. Here absolute and relative intensity distributions of electronic, vibrational and rotational structures of measured spectra contain information on plasma processes and properties. The spectral resolutions needed, e.g., for determining the rotational and electronic distributions differ by two orders of magnitude. When using ordinary diffraction gratings this causes some inconvenience not present with the use of a modern broadband echelle spectrometer. However, some unusual properties of these spectrometers must be taken into account. We utilize such a spectrometer for the diagnostics of gas discharges employed in diverse branches of plasma technology. In this paper we describe its relative and absolute calibrations and discuss some specific problems connected with these calibrations and with using this type of spectrometer.

## 2. The UV/VIS echelle spectrometer ‘Spectra Analyser ESA 3000’

For our investigations we use the Spectra Analyser ESA 3000<sup>®</sup>, a broad-range spectrometer originally developed for applications such as laser-induced breakdown spectroscopy. In this kind of instrument typically a wavelength range from 200 nm to 800 nm is simultaneously displayed in more than 90 spectral orders and at a resolution of a few picometres. The scheme of a modern broadband echelle spectrometer is presented in figure 1. Light enters via an optical fibre (not shown in figure 1), the exit of this fibre acting as a secondary light source in front of the entrance slit of the spectrometer. The width of the entrance slit is fixed. The echelle grating is also fixed and arranged under a flat angle of incidence. It produces more than 90 overlapping diffraction orders. A quartz prism in front of the grating separates these orders. The dispersion of this prism acts in a direction perpendicular to the direction of the grating’s dispersion and thus forms the spectrum as a two-dimensional pattern. In this way the compact spectrograph covers a total spectrum length of over 1 m folded to a 25 mm × 25 mm area in the focal plane, the

position of the CCD-detector. Thus the spectrometer achieves high resolution and parallel detection of nearly all analytical lines of interest together with their spectral background.

Coupling the CCD-detector array with an image intensifier enables measuring very weak light sources as well as short light pulses (decay measurements). When electric signals gate the image intensifier (amplification up to 10<sup>4</sup>), it works like an extremely fast camera shutter. This offers the possibility of synchronizing the measurements with an external electrical signal both in the ‘master’ and in the ‘slave’ mode and in a very broad range of time variations. Time resolutions down to 20 ns are possible [1]. Further, the system exhibits a very low stray light level and a high throughput in the UV.

These properties are also helpful for plasma diagnostics, as plasma is often neither homogeneous nor stationary. For obtaining spatial resolution a diaphragm must limit the solid acceptance angle of the optical fibre constituting the spectrometer entrance. We use diaphragms with three different openings and measured the (solid) acceptance angles of the fibre. Thus we found an angular acceptance following in good approximation a cosine function.

Because of its action as a secondary light source the optical fibre offers the big advantage of illuminating the grating always in a well-defined way. Thus it is much easier to compare the illumination by calibration light sources and by a light source (e.g. a discharge) under investigation. The tedious procedure of arranging the system for equal acceptance angles, as in the case of spectrometers where the entrance slit is directly illuminated (see, e.g., [2]), is not needed.

The spectrometer works in the (echelle diffraction grating) spectral orders 30 to 120. Over the spectrum, therefore, the angle dispersion  $d\varphi/d\lambda$  of the echelle (and correspondingly the linear dispersion  $dx/d\lambda$ ) follows fairly accurately the relation

$$\frac{d\varphi}{d\lambda} = \frac{n \cdot g}{\cos \varphi}. \quad (1)$$

Here  $n$  is the spectral order,  $g$  the groove density ( $g = 75$  grooves per mm in our case),  $\varphi$  the angle of deflection with respect to the surface normal ( $\varphi \approx 60^\circ$ ; see discussion below) and  $\lambda$  the wavelength.

The efficiency of the spectrometer depends mainly on the blazing of the grating and on the sensitivity of the photon detector. Regardless of the fact that any variation of the deflection angle is small ( $\leq 2^\circ$ ), the reflection coefficient of the grating changes considerably on the borders of each spectral order. Thus the efficiency of the spectrometer decreases in the respective spectral regions. Furthermore, as the deflection angle differs from  $90^\circ$ , within a certain spectral order any small change of the deflection angle, according to equation (1), causes a remarkable change of the dispersion. If we proceed from the spectral  $n = 100$  to  $n = 101$ , for example, the dispersion changes by 1%, while the change caused by the varying deflection angle within one spectral order amounts to 6%.

These variations of efficiency and dispersion introduce some calibration and measurement problems. For example, in the 91 spectral regions of the ESA 3000 (corresponding to the 91 spectral orders) the wavelength range  $\Delta\lambda_{\text{pixel}}$  covered by one pixel varies from  $\Delta\lambda_{\text{pixel}} = 5$  pm at  $\lambda = 200$  nm to  $\Delta\lambda_{\text{pixel}} = 20$  pm at  $\lambda = 800$  nm as the width of a CCD pixel is 24  $\mu\text{m}$  and constant over the entire CCD chip. The spectral

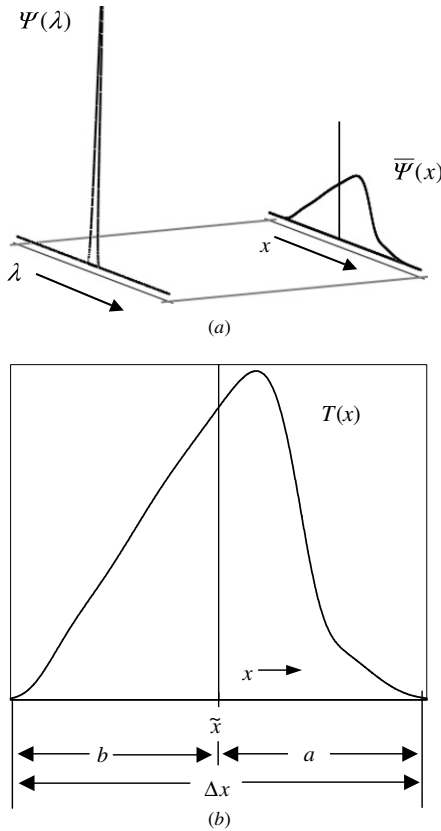


**Figure 2.** (a) Transformation of a spectral line into a spatial intensity distribution on the EAS 3000 detector surface (schematic). (b) Instrumental function  $T(x)$  (schematic).

resolution defined as the half-width of a narrow atomic line equals about 15 pm at  $\lambda = 200$  nm and 60 pm at  $\lambda = 800$  nm. While even for the lowest spectral orders the spectral ranges do not overlap, above 500 nm there are some narrow spectral bands where the spectrometer efficiency is zero. Despite the fact that the spectral range covered by these zero efficiency bands all together amounts only to less than 10% of the total range, one must be aware that some lines may disappear from the spectrum.

### 3. Transformation of optical radiation within the spectrometer

#### 3.1. Generalities

Any spectrometer transforms a spectrum, that is, a certain spectral distribution of light,  $\Psi(\lambda)$ , into a local distribution  $\bar{\Psi}(x)$  (see figure 2(a)). Here  $x$  is the lateral coordinate on the optical detector, in the case of the ESA 3000 a CCD-chip. The transformation involves two effects: dispersion and optical imaging. The dispersive element, the grating, reflects incoming light waves. The grating is combined with two spherical mirrors producing for each wavelength an optical image of the entrance slit on the plane of the optical detector, as depicted in figure 1. The totality of these images represents the optical spectrum, one image a spectral line.

We describe the transformation process in the spectrometer by an instrumental function  $T(x)$ , with

$\int T dx = 1$ , and an efficiency function  $\Phi(\lambda)$ . Determining  $\Phi(\lambda)$  is the aim of the calibration procedure, the function  $T(x)$  defines the spectral resolution.

We assume illumination of the entrance slit by a photon flux  $\Psi$ . Thus the amount of light with a certain wavelength  $\tilde{\lambda}$  is given by  $d\Psi(\tilde{\lambda}) = d\Psi/d\lambda|_{\tilde{\lambda}} d\lambda$ . Here  $d\Psi/d\lambda$  is the spectral density of the incoming light flux.

This flux is attenuated on its way to the optical detector. That attenuation we describe by the attenuation function  $\Phi_s(\lambda)$ . Thus the optical detector is hit by a flux

$$d\bar{\Psi} = \Phi_s(\tilde{\lambda}) \cdot d\Psi. \quad (2)$$

The flux  $d\bar{\Psi}$  is distributed over a certain region of the detector anchored at a coordinate  $\tilde{x}$  (see figure 2(b)). The coordinate  $\tilde{x}$  is determined by  $\tilde{\lambda}$  via the dispersion function  $x(\lambda)$  of the optical system of the spectrometer. To derive an expression for this dispersion relation we consider the situation in one single spectroscopic order  $n$  (with  $30 \leq n \leq 120$ ). Let  $f$  be the focal distance of the spherical mirror ( $f = 0.25$  m) and  $\alpha$  and  $\varphi$  the incident and deflection angles. Those of these angles corresponding to  $\lambda_n$ , the central wavelength of a spectral order, we denote by  $\alpha_n$  and  $\varphi_n$ . For any order  $n$ , we have  $\alpha_n = 67.1^\circ$  and  $\varphi_n = 61.5^\circ$ . We define a specific space coordinate  $x$  by  $x(\lambda_n) = 0$  and describe the deflection by the angle  $\theta = \varphi - \varphi_n$ . Thus  $\theta = 0$  for  $x = 0$  and  $|\theta_{\max}| \leq 1^\circ$ . With these premises we obtain as the condition of constructive interference

$$\lambda \cdot n \cdot g = \sin(\varphi_n + \theta) + \sin \alpha_n \quad (3)$$

and within the approximation of Gaussian optics

$$x(\lambda) = f \cdot \tan \theta. \quad (4)$$

Solving for  $\sin \theta$  we obtain from equation (3)

$$\sin \theta = \frac{\lambda \cdot n \cdot g}{\cos \varphi_n} + \frac{\theta^2 \cdot \tan \varphi_n}{2} - \frac{\sin \alpha_n}{\cos \varphi_n} - \tan \varphi_n. \quad (5)$$

Here we have used the approximation  $\cos \theta = 1 - \frac{\theta^2}{2}$  (systematic error  $< 0.06\%$ ). If in equation (4) we approximate  $\tan \theta$  by  $\sin \theta$  (systematic error  $< 0.08\%$ ) and introduce this into equation (5), we obtain for the dispersion function of the spectrometer

$$x(\lambda) = f \cdot \left( \frac{\lambda \cdot n \cdot g}{\cos \varphi_n} + \frac{\theta(\lambda)^2 \cdot \tan \varphi_n}{2} - \frac{\sin \alpha_n}{\cos \varphi_n} - \tan \varphi_n \right). \quad (6)$$

With  $\frac{d\theta(\lambda)}{d\lambda} = \frac{d\varphi}{d\lambda} \approx \frac{n \cdot g}{\cos \varphi_n}$  the linear dispersion is given by

$$\begin{aligned} \frac{dx}{d\lambda} &= \frac{f \cdot n \cdot g}{\cos \varphi_n} + f \cdot \theta(\lambda) \cdot \frac{d\theta(\lambda)}{d\lambda} \cdot \tan \varphi_n \\ &= \frac{f \cdot n \cdot g}{\cos \varphi_n} (1 + \theta(\lambda) \cdot \tan \varphi_n). \end{aligned} \quad (7)$$

At the edges of a spectral order the second term in the rhs brackets contributes at maximum about  $\pm 3\%$ , independently of the spectral order  $n$ .

That (differential) part of the light flux  $d\bar{\Psi}(\tilde{\lambda})$ , which hits at a position  $x$  the detector on a differential stripe  $dx$ , is given by

$$d(d\bar{\Psi}) = \Phi_s(\tilde{\lambda}) \cdot d\Psi \cdot T(x - \tilde{x}(\tilde{\lambda})) dx. \quad (8)$$

The detector transforms the photon flux  $d(d\bar{\Psi})$  into an electrical signal  $d(dI(x))$ , for which we obtain

$$\begin{aligned} d(dI(x)) &= \Phi_P(x, \tilde{\lambda}) \cdot d(d\bar{\Psi}(\tilde{\lambda})) \\ &= \Phi_P(x, \tilde{\lambda}) \cdot \Phi_s(\tilde{\lambda}) \cdot d\Psi \cdot T(x - \tilde{x}(\tilde{\lambda})) dx. \end{aligned} \quad (9)$$

Here  $\Phi_P(x, \tilde{\lambda})$  is the detector's wavelength dependent quantum efficiency for the wavelength  $\tilde{\lambda}$  at the location  $x$ .

However,  $d(d\bar{\Psi}(\tilde{\lambda}))$  is not the only contribution to the photon flux hitting the detector between  $x$  and  $x + dx$ . Any wavelength for which the product of the instrumental function  $T$  with the differential flux  $d\Psi$  attains a non-zero value at  $x$ , will contribute as well. For a given  $x$  the instrumental function  $T$  extends over a range  $\Delta x = a + b \approx 120 \mu\text{m}$  (that is over five pixels, as discussed below). Here  $a$  and  $b$  represent the distances between  $\tilde{x}$  and the right, respectively the left, border of the range, where  $T(x) \neq 0$  as shown in figure 2(b). Thus the total signal  $dI(x)$  stemming from the differential stripe  $dx$  is due to the contributions of light with any wavelength  $\tilde{\lambda}$ , for which  $x - \tilde{x} \leq a$  or  $\tilde{x} - x \leq b$ . This corresponds to an interval of  $\tilde{x}$  given by  $x - a \leq \tilde{x} \leq x + b$ . Here we have assumed—as usual—that the true wavelength  $\tilde{\lambda}$  of a line is in the middle of the interval defining the measured halfwidth of that line (nevertheless we may have  $a \neq b$ ). Thus we obtain for  $dI(x)$ , the signal due to the total light hitting the considered stripe

$$dI(x) = \left[ \int_{\lambda(x-a)}^{\lambda(x+b)} \Phi_P(x, \tilde{\lambda}) \cdot \Phi_s(\tilde{\lambda}) \cdot T(x - \tilde{x}(\tilde{\lambda})) \frac{d\Psi}{d\lambda} \Big|_{\tilde{\lambda}} d\tilde{\lambda} \right] dx. \quad (10)$$

The limits of this integral must be determined by the dispersion relation because the extension of  $T(x)$  does not depend on the wavelength. The detector consists of discrete pixels, each having an extension  $\Delta = 24 \mu\text{m}$ . The spectral width of a pixel

$$\Delta\lambda_{\text{pixel}} = \Delta \cdot \left( \frac{dx}{d\lambda} \right)^{-1} \quad (11)$$

depends on the dispersion relation which is, according to (7), on the spectral order  $n$  and on the value of the refraction angle  $\theta$ .

Every pixel gives an electrical signal  $I(X)$ . Here  $X$  is a discrete variable indicating the location of a pixel on the  $x$ -scale:

$$I(X) = \int_{\text{pixel}} dI(x) = \int_{\text{pixel}} \left[ \int_{\lambda(x-a)}^{\lambda(x+b)} \Phi_P(x, \tilde{\lambda}) \cdot \Phi_s(\tilde{\lambda}) \times T(x - \tilde{x}(\tilde{\lambda})) \cdot \frac{d\Psi}{d\lambda} \Big|_{\tilde{\lambda}} d\tilde{\lambda} \right] dx. \quad (12)$$

For further discussions, we consider the two limiting cases of (almost) monochromatic line radiation and continuum radiation.

### 3.2. Continuum radiation

If over the wavelength ranges covered by one pixel and/or by the instrumental function the changes of the spectral density are very small, we may approximate equation (12) by

$$I(X) \approx \frac{d\Psi}{d\lambda} \Big|_{\tilde{\lambda}} \cdot \int_{\text{pixel}} \left[ \int_T \Phi_P(x, \tilde{\lambda}) \cdot \Phi_s(\tilde{\lambda}) \times T(x - \tilde{x}(\tilde{\lambda})) d\tilde{\lambda} \right] dx = \frac{d\Psi}{d\lambda} \Big|_{\tilde{\lambda}} \cdot \langle \Phi_P(x, \lambda) \cdot \Phi_s(\lambda) \rangle_{T \oplus \text{pixel}} \cdot \Delta\lambda_{\text{pixel}}. \quad (13)$$

Thus  $I(X)$  depends on the dispersion relation. Therefore, due to the pixel structure of the detector, the efficiency functions, obtained by means of a continuous light source, will also depend on the linear dispersion of the spectrometer. If it is possible to rule out dramatic changes of  $d\Psi/d\lambda$ ,  $\Phi_s$  and/or  $\Phi_P$  over this wavelength range, the integrations over  $x$  and  $\tilde{\lambda}$  are equivalent. This means that in the continuum case due to the contributions of radiation with wavelengths neighbouring  $\tilde{\lambda}$  the signal of one single pixel is equivalent to an integral of the signals caused by the monochromatic  $\tilde{\lambda}$ -radiation distributed over the entire extension of  $T(x - \tilde{x}(\tilde{\lambda}))$ .

### 3.3. Line radiation

In the case of radiation consisting of isolated (almost) monochromatic spectral lines we can approximate the flux of the incoming light by

$$\Psi_{\text{line}}(\tilde{\lambda}) = \int \frac{d\Psi}{d\lambda} d\lambda = \int \Psi_{\text{line}}(\tilde{\lambda}) \cdot \delta(\lambda - \tilde{\lambda}_{\text{line}}) d\lambda, \quad (14)$$

where  $\delta$  represents Dirac's  $\delta$ -function,  $\tilde{\lambda}_{\text{line}}$  is the (central) wavelength of the considered spectral line. Introducing this into equation (12) we obtain for a certain pixel, say at  $X_i$ , after integration over  $\lambda$ :

$$I_i = I(X_i) = \Phi_s(\tilde{\lambda}_{\text{line}}) \cdot \Psi_{\text{line}}(\tilde{\lambda}_{\text{line}}) \times \int_{\text{pixel}} \Phi_P(x, \tilde{\lambda}_{\text{line}}) \cdot T(x - \tilde{x}(\tilde{\lambda}_{\text{line}})) dx. \quad (15)$$

In our case  $T$  covers five to six pixels and we obtain the signal produced by the entire line as a sum of the signals dispensed by those pixels,

$$I_{\text{line}} = \sum_{\text{line}} I_i = \Phi_s(\tilde{\lambda}_{\text{line}}) \cdot \Psi_{\text{line}}(\tilde{\lambda}_{\text{line}}) \times \int_T \Phi_P(x, \tilde{\lambda}_{\text{line}}) \cdot T(x - \tilde{x}(\tilde{\lambda}_{\text{line}})) dx = \Psi_{\text{line}}(\tilde{\lambda}_{\text{line}}) \cdot \Phi_s(\tilde{\lambda}_{\text{line}}) \cdot \sum_{\text{line}} \langle \Phi_P(X_i, \tilde{\lambda}_{\text{line}}) \rangle_{\text{pixel}} = \Psi_{\text{line}}(\tilde{\lambda}_{\text{line}}) \cdot \Phi_s(\tilde{\lambda}_{\text{line}}) \cdot \langle \Phi_P(X, \tilde{\lambda}_{\text{line}}) \rangle_T. \quad (16)$$

For the case considered we obtain in (16) the total signal  $I_{\text{line}}$  due to a spectral line as the product of the total radiation  $\Psi_{\text{line}}(\tilde{\lambda}_{\text{line}})$ , with  $\Phi_s$  for the line wavelength  $\tilde{\lambda}_{\text{line}}$  and the average of  $\Phi_P$  for this same wavelength over the range of the instrumental function  $T$ . Apart from the averaging of  $\Phi_P$  the signal  $I_{\text{line}}$  does *not* depend on the dispersion relation. (Strictly speaking,  $\Phi_s$  also is an average, but over the wavelength range of the spectral line at that.)

In figures 3(a) and (b) we show the pixel signals due to the narrow Ar I lines at 794.82 nm, respective at 750.39 nm as column-plots. The differences in these column-plots are due to small differences in the relative position of  $\tilde{x}$  with respect to the central pixels and to the superposition of very weak background lines. These plots represent the only type of information available on the instrumental function  $T$ . The  $X$ -coordinate is here—via the dispersion relation—replaced by a wavelength scale (in our case this is automatically performed by the software used to run ESA 3000). We have constructed the shape of  $T$  presented in figure 2(b) in such a way that a simulation of the pixel-integration yields a closely similar

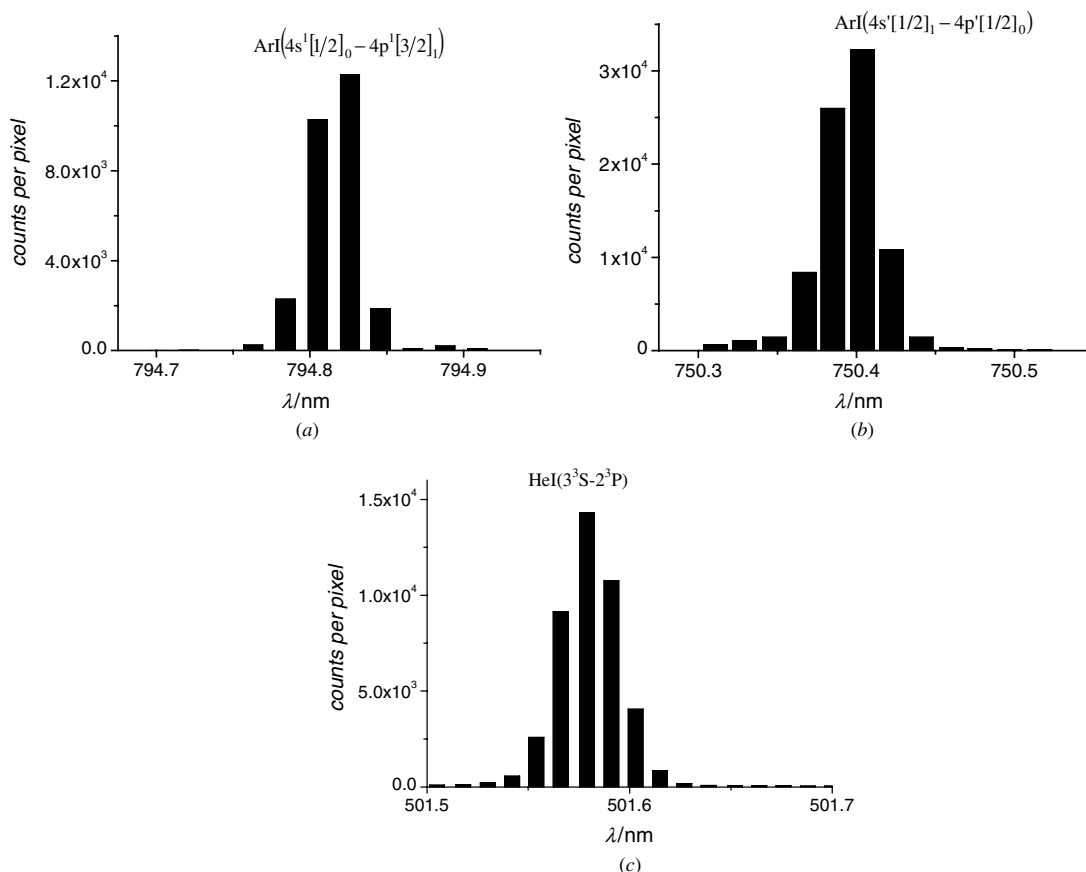


**Figure 3.** (a), (b) Measured narrow Ar I lines. The columns represent a picture of the instrumental function  $T$ , integrated over the respective pixels. The differences between (a) and (b) come from slight differences in the positions of the respective wavelengths  $\tilde{\lambda}$  relative to the pixels. (c) Measured ‘broad’ He I line (unresolved triplet) with a width almost equal to the halfwidth of  $T$ .

picture. But this does not necessarily mean that the function shown in figure 2(b) represents the real  $T$ .

If the linewidth of a line is of the same order of magnitude as the instrumental function or even larger, we obtain as the general case the signal as a convolution between line shape and instrumental function, as shown in figure 3(c). The presented He I-line is an unresolved superposition of three fine-structure components of a line-triplet and thus much broader than the Ar I lines in figures 3(a) and (b). Its width is of the same order of magnitude as that of  $T$ . In this case we have to use equation (12) instead of (16) because the simplifications introduced in equations (14)–(16) are not valid; see discussion below.

### 3.4. Discussion

If we define an experimental correction function  $\varepsilon_{\text{exp}}(\tilde{\lambda})$  as the ratio between the spectrometer signal and the spectral quantity to be measured, we see that in the case of continuum radiation such a function may be defined as

$$\begin{aligned} 1/\varepsilon_{\text{exp}}(\tilde{\lambda}) &= I(X) \left/ \frac{d\Psi}{d\lambda} \right|_{\tilde{\lambda}} \\ &= \Delta\tilde{\lambda}_{\text{pixel}} \cdot \langle \Phi_P(x, \lambda) \cdot \Phi_S(\lambda) \rangle_{T \oplus \text{pixel}}, \end{aligned} \quad (17)$$

that is, as an average of the product  $\Phi_P \cdot \Phi_S$  over a range defined by the range of one pixel plus the instrumental width.

Structures of the efficiency function (holes, steps etc) are smeared out over this range. Structures of  $d\Psi(\lambda)/d\lambda$  (lines, steps, shoulders) will be smeared out as well. In this latter case the value of  $\varepsilon_{\text{exp}}$  may be influenced by such a structure in a non-predictable way and not only reflect the efficiency function. It, therefore, is problematic to eliminate, say, a superimposed line by simply cutting it from  $d\Psi(\lambda)/d\lambda$ , because its influence on  $I(X)$  may extend over a range that is enlarged by the averaging process.

If we try to define a correction function for line radiation by using equation (16), we obtain

$$I_{\text{line}}/\Psi_{\text{line}} = \Phi_S(\tilde{\lambda}_{\text{line}}) \cdot \langle \Phi_P(X, \tilde{\lambda}_{\text{line}}) \rangle_T. \quad (18)$$

As discussed above, this expression does not depend on the dispersion relation. Apart from the somewhat different averaging of the right side, it further differs from the expression given in equation (17) by its denominator, which is a radiation flux instead of a spectral density. Thus calibrations based on these different expressions cannot be directly compared. However, the denominator of the lhs in equation (18) corresponds to an integration over  $\lambda$  of the denominator of the lhs in equation (17). We therefore obtain an expression equivalent to equation (17) by replacing  $I_{\text{line}}$  by an integration over the pixel signals defined in (16) by  $\int_{\text{line}} I d\lambda \approx I_{\text{line}} \cdot \Delta\lambda_{\text{pixel}}$ . This same formula can be used in the case of lines composed out of unresolved components such as the He-line displayed in figure 3(c).

As according to equation (11) the range  $\Delta\lambda_{\text{pixel}}$  depends on the wavelength, line spectra corrected by means of such efficiency functions obtained from continuum radiation do not reflect the true spectral distribution of a line. Only the sum  $I_{\text{line}} = \sum_{\text{line}} I_i \propto I_{\text{line}} \cdot \Delta\lambda_{\text{pixel}}$  as defined in equation (16) gives correct information on the intensity of the corresponding emission transitions. (Due to the proportionality between  $I_{\text{line}}$  and  $\int_{\text{line}} I d\lambda$  the latter can be used for the relative as well as for the absolute calibration.) This fact must be taken into account when comparing emission spectra measured by different spectrometers, when determining atomic or molecular parameters like, say, the dipole-momentum function for emission transitions of two-atomic molecules, when determining the gas temperature by means of OES etc. In the two latter cases the required parameters are determined by fitting a calculated spectral intensity distribution to a measured one (see [3, 4]). For this purpose the measured emission spectra must be corrected for the spectrometer efficiency, and if this efficiency function is determined by means of a continuous light source the influence of the linear dispersion must be taken into account. This is one of the most significant problems when working with broadband spectrometers such as the ESA 3000.

Also other types of broadband spectrometers, working in the first spectral order of the diffraction grating, have a similar problem, although its effect is not as serious. For determining the efficiency function one often (or even as a rule) uses the continuum emission of a tungsten-ribbon or deuterium lamp, or synchrotron radiation. In these spectrometers, because of working in only one spectral order, the deflection angle  $\varphi$  varies continuously with the wavelength within wide limits. Thus the angle dispersion and the wavelength range covered by a pixel depend on the deflection angle (see (1)), that is on the wavelength. For example, for the 15 cm focal length ARC SpectraPro-150 spectrometer with a diffraction grating with 1200 grooves  $\text{mm}^{-1}$   $\Delta\lambda_{\text{pixel}}$  amounts to 0.06 nm/pixel at 200 nm and to 0.04 nm/pixel at 800 nm. For the 50 cm spectrometer ARC SpectraPro-500i with a grating with 1800 grooves  $\text{mm}^{-1}$  the respective values are 0.02 nm/pixel at 200 nm and 0.013 nm/pixel at 800 nm. As for the echelle spectrometer these spectrometers yield the true intensity ratios of lines or lines and continuum radiation only if the integral intensities of the lines are used. The relations between line maxima or between line maxima and the intensity of a continuum may deviate from those ratios.

## 4. Relative and absolute calibration

### 4.1. Procedure and results

We want to use the echelle spectrometer for the diagnostics of gas discharges of technical relevance. For this purpose we need the absolute intensities (unit: photons  $\text{s}^{-1}$ ) of the emission spectra. Any calibration proceeds by comparing a measured spectrum of a standard source with the known intensity distribution of this source. The relative and absolute efficiency functions are obtained as a ratio between the ideal and measured spectra. This requires a perturbation-free measurement. The photon detector counts single photons. Thus at too low counting rates problems may arise from statistical errors, at too high counting rates from local memory

overflow. It is almost impossible to find a standard light source covering the entire spectral range of a broadband echelle and circumventing these problems. A further problem comes from using many spectral orders at the same time, because the efficiency will be very small at the borders of the spectral orders. Thus the efficiency function is strongly structured. To cope with these structures the standard light source must emit a continuous spectrum. If it also contains some narrow lines, smoothing the measured spectrum during the calibration procedure eliminates these lines. These problems are common to all types of broadband echelle spectrometers using a similar photon detector. Our strategy for circumventing these problems and described in the following sections may be specific to the ESA 3000 used in our calibration and may need modifications when using a different type.

The ESA 3000 system includes software, which offers the possibility for correcting the measured spectra directly after measurement or after reading them from the HD. A correction function  $\varepsilon(\lambda) \propto 1/\Phi(\lambda)$  can be produced by a calibration procedure, started by pushing a button. According to the EAS 3000 manual,  $\varepsilon(\lambda)$  is apt for a *relative* calibration and therefore proportional (not equal) to  $1/\Phi$ . One single standard light source is needed, which covers the entire spectral range of interest. The known intensity distribution of this (secondary) standard must be stored in the memory of the system together with its actually measured emission spectrum. After starting the calibration procedure the system produces the correction function  $\varepsilon(\lambda)$  over the range of the measured spectrum and stores it automatically. It is not possible to compose a calibration function directly out of parts obtained from different standard lamps, covering different spectral ranges.

For our calibration we had at our disposal a tungsten-ribbon lamp absolutely calibrated in the spectral region  $270 \text{ nm} \leq \lambda \leq 800 \text{ nm}$ , a highly stable Xe lamp type (Hamamatsu<sup>®</sup>, L2273, 150 W,  $185 \text{ nm} \leq \lambda \leq 2000 \text{ nm}$ , output drift below  $\pm 0.5\%$  per hour) and a deuterium lamp (Hamamatsu<sup>®</sup>, L1728, 30 W,  $185 \text{ nm} \leq \lambda \leq 450 \text{ nm}$ , output drift below  $\pm 0.5\%$  per hour). The xenon lamp covers more than the entire spectral range of the spectrometer. We, therefore, in a first attempt, performed a relative calibration of this lamp and tried to use it as a secondary standard. The spectrometer collects a spectrum in a pre-settable time interval and stores it in a memory. The memory will overflow locally if the signal from one pixel exceeds  $6 \times 10^4$  counts. Due to statistical fluctuations of the counting rate this implies saturation effects beginning at an average of about  $4 \times 10^4$  counts per pixel in the respective spectral region (our spectrometer indicates such an overflow by a warning on the screen used for displaying the spectra). We produced a correction function  $\varepsilon(\lambda)_{\text{Xe}}$  with spectrometer settings avoiding overflow. For controlling  $\varepsilon(\lambda)_{\text{Xe}}$  we measured the spectrum of the deuterium lamp and corrected it with this function. In the UV-region of the corrected spectrum we observed artefacts displayed in figure 4. The D<sub>2</sub>-lamp emits no lines in the displayed spectral range (see the respective wavelength range in figures 6 and 9. In the spectra displayed in these figures, the radiation below 220 nm is entirely due to the deuterium lamp). The peaks showing up at regular intervals indicate the low efficiency zones at the borders between two spectral orders. At these borders some complementary corrections of the efficiency function are implemented in the algorithm

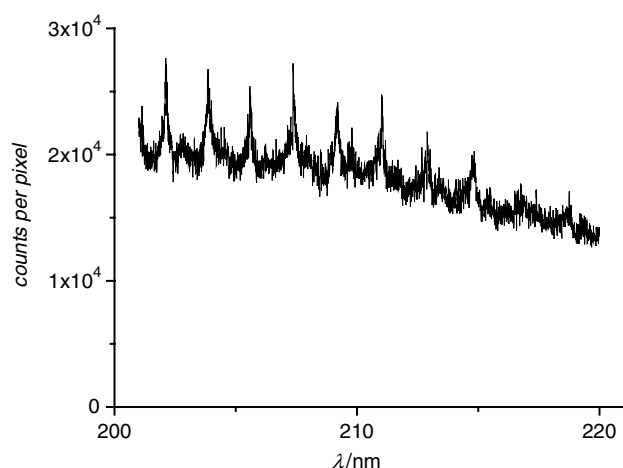


**Figure 4.** Part of a measured continuous deuterium emission spectrum corrected by means of a correction function obtained by a Xe lamp as secondary standard. The ‘lines’ are artefacts (see discussion in text).

for generating the correction function, because the smoothing procedure distorts the efficiency function near jumps of the slope of the efficiency. The low UV-intensity of the Xe-lamp together with the low counting efficiency of the spectrometer at the borders of the spectral orders results in such low counting rates that statistical errors falsify the correction procedure. Thus the function  $\varepsilon(\lambda)_{\text{Xe}}$  systematically

underestimates the spectrometer efficiency in this region and, therefore, overcorrects the counting rates.

Because of the narrow regions with low counting rates this produces lines as artefacts. They disappear where—during calibration—the number of counts from one pixel exceeded a certain limit. Experimentally we found that to avoid the perturbation at least  $3 \times 10^3$  counts per any pixel must be gathered in the calibration process. To prevent respective calibration errors and/or errors caused by memory overflow, one needs a standard light source having over the entire range of the spectrometer an intensity variation so small that the CCD output of counts varies by less than a factor 10–12. For our standard lamps this condition is fulfilled only over limited ranges: at the ‘standard’ setting of the spectrometer for the band lamp from 400 nm to 800 nm, for the Xe-lamp from 270 nm to 750 nm, and for the deuterium lamp from 200 nm to 450 nm. Therefore, none of these light sources can be used for relatively calibrating the entire range of the spectrometer.

However, the deuterium lamp with any of the two other lamps will cover the entire wavelength-region with overlapping ranges. We, therefore, coupled the standard tungsten lamp with the deuterium lamp in the arrangement displayed in figure 5: the two light sources are coupled by means of a quartz plate. We used the spherical mirror and the quartz lens for focusing the photon fluxes on the entrance hole of the optical fibre serving as the entrance of the spectrometer. By varying the position of the quartz lens we reduced the photon flux from the deuterium lamp by defocusing its image. Thus we obtained a ‘composite’

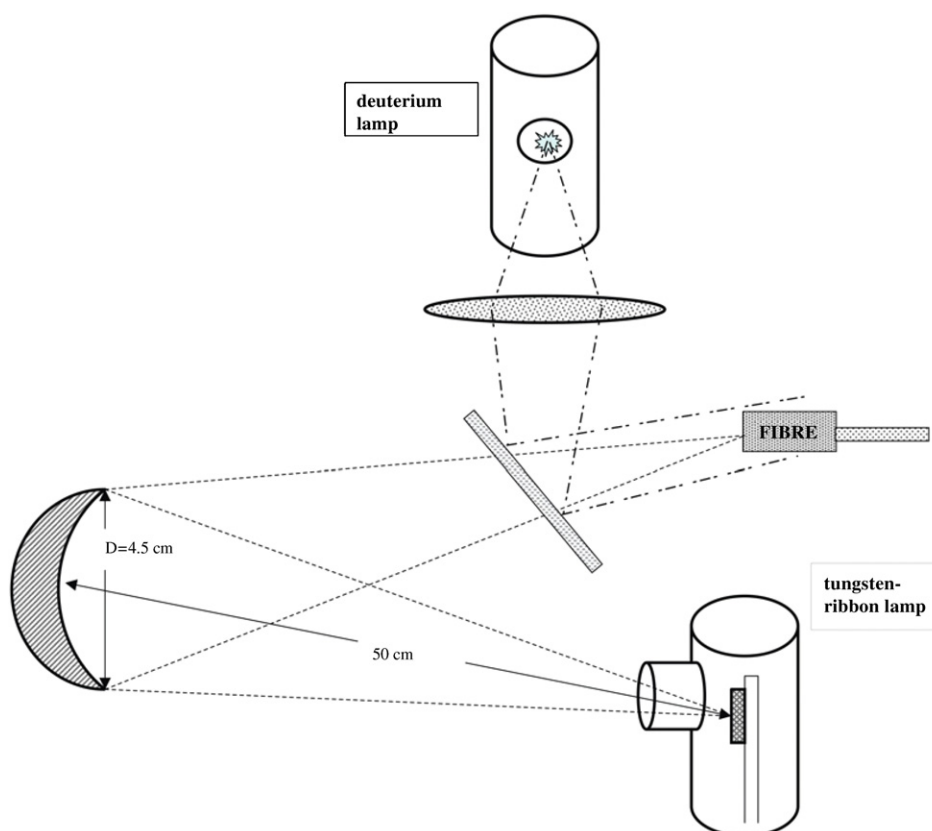


**Figure 5.** Optical scheme of an adjustable ‘composite’ light source for a relative calibration of the spectrometer (see text).

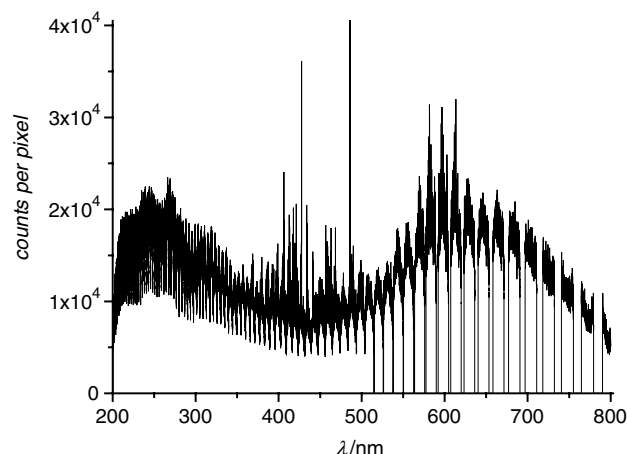


**Figure 6.** The uncorrected spectrum of the light source from figure 5 showing that the spectrometer output varies in the limits between  $3 \times 10^3$  and  $4 \times 10^4$  counts per pixel.

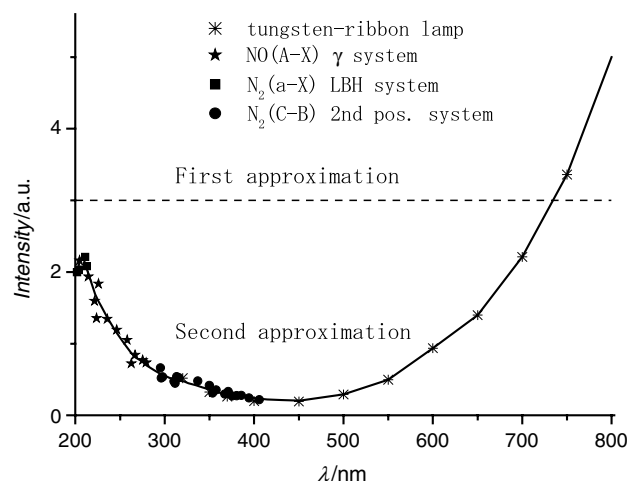


**Figure 7.** ‘True intensity distributions’ of the standard spectrum from the composite light source of figure 5 used for the relative calibration of the spectrometer (see text for details).

spectrum fulfilling the condition discussed above (except for the zero efficiency zones of the spectrometer). Commercially available tungsten-deuterium lamps are combinations of a deuterium lamp and a tungsten ribbon lamp. They can be used in a similar way, when adjusting the operational parameters in a proper way. We think that our ‘composite’ light source offers greater flexibility. We present our results in figure 6 as the non-processed spectrum obtained from our composite lamp. To determine the true intensity distribution of this source we used the following procedure:

- (a) In a first step we stored as the ‘true intensity distribution’ of our composite lamp a constant value over the entire spectral region  $200 \text{ nm} \leq \lambda \leq 800 \text{ nm}$  in the respective memory and performed the calibration procedure of the spectrometer with this premise (see figure 7). In this way we obtained an uncalibrated ‘correction function’  $\varepsilon(\lambda)_{\text{uncorr}}$ . It already contains the structure due to the spectral orders and is free of distortions by statistical errors or overflow. In the following steps we describe the calibration of  $\varepsilon(\lambda)_{\text{uncorr}}$ .

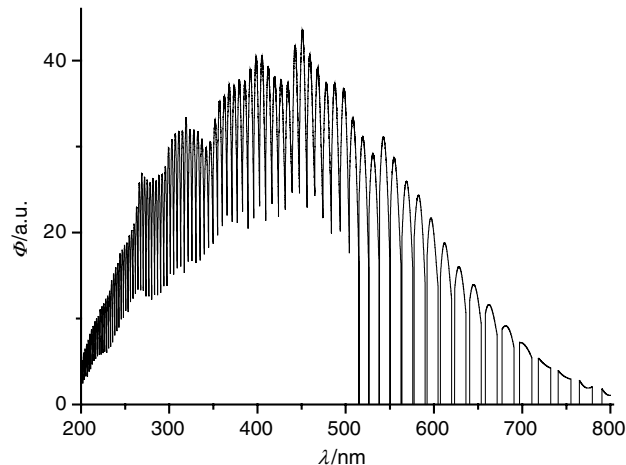


**Figure 8.** Relative efficiency  $\Phi(\lambda) = 1/\varepsilon(\lambda)$  of the spectrometer ESA 3000 obtained by the calibration procedure (see text for details).

- (b) Then we measured the well-known spectra of the tungsten-ribbon lamp ( $300 \text{ nm} \leq \lambda \leq 800 \text{ nm}$ ) and the following molecular spectra emitted by an RF discharge: the NO( $A^2\Sigma^+ - X^2\Pi$ )  $\gamma$ -system ( $200 \text{ nm} \leq \lambda \leq 300 \text{ nm}$ ), the N<sub>2</sub>( $C^3\Pi_u - B^3\Pi_g$ ) ‘second positive’ system ( $280 \text{ nm} \leq \lambda \leq 450 \text{ nm}$ ) and the N<sub>2</sub>( $a^1\Pi_g - X^1\Sigma_g^+$ ) Lyman–Birge–Hopfield (LBH) system (available with this spectrometer in the range  $200 \text{ nm} \leq \lambda \leq 220 \text{ nm}$ ). We ‘corrected’ these spectra by the correction function  $\varepsilon(\lambda)_{\text{uncorr}}$  obtained in step (a).
- (c) We compared the intensity distributions of the spectra obtained (in the case of line spectra as integrals over the measured line profiles) in step (b) with the well-known spectra of these radiation sources and determined (relative) correction factors linked by the overlapping spectral regions.
- (d) We corrected the ‘true intensity distribution’ assumed in step (a) by the correction factors from step (c)—see figure 7—and repeated the calibration procedure with the originally measured spectrum of the composite lamp and this new standard spectrum. In this way we obtained instead of  $\varepsilon(\lambda)_{\text{uncorr}}$  the final correction function  $\varepsilon(\lambda)$ . The respective efficiency function corresponding to the blaze of the grating in the spectral range of each spectral order,  $\Phi(\lambda)$ , is displayed in figure 8.

By using  $\varepsilon(\lambda)$  to correct the unprocessed spectrum of figure 6 we obtained also the correct spectrum of the ‘composite’ light source of figure 5; see figure 9.

The optical setup of figure 5 is thus used for transferring and normalizing relative correction functions from different light sources. After this procedure the echelle spectrometer (together with our composite lamp) is calibrated against emission spectra of two-atom molecules (branching ratio method, see discussion below) and the standard tungsten-ribbon lamp. The uncertainties of the standard spectrum in figure 7 amount to 5%, 9%, 10%, 9%, and 6% for the ranges 200–250 nm, 250–300 nm, 300–350 nm, 350–400 nm and 400–800 nm, respectively. The corrected spectrum of our composite light source shown in figure 9—within the limits

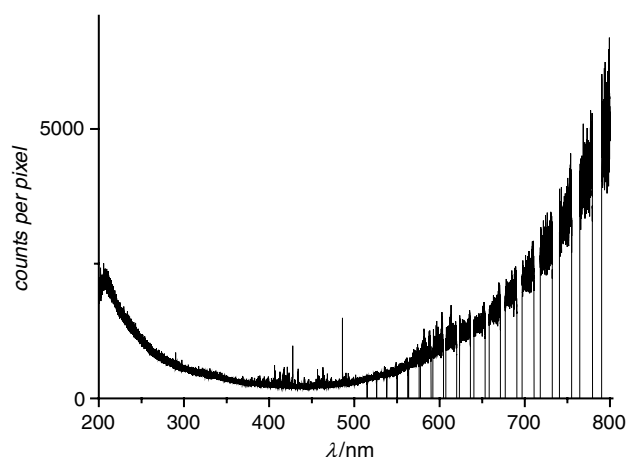


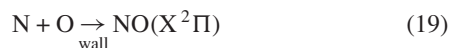
**Figure 9.** The spectrum of figure 6 corrected by  $\varepsilon(\lambda)$ . Compare figure 4 and the second approximation in figure 7: the artificial lines below 220 nm disappeared, the spectrum equals the second approximation in figure 7 except for the noise.

of the statistical fluctuations of the measured signal—is equal to the standard spectrum in figure 7. The artificial peaks in the UV-region presented in figure 4 do not show up. For a consistency check we measured and corrected the spectra of the light sources used in step (b) and found agreement with their theoretical intensity distributions. In the range  $200 \text{ nm} \leq \lambda \leq 210 \text{ nm}$ , where counting rates are low, the systematic errors at the borders of the spectral orders are below 10% (see figure 8).

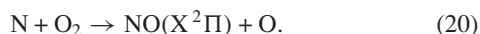
#### 4.2. Discussion of the branching-ratio method used for calibration

The branching-ratio method results in a series of benchmarks (corresponding to the individual lines), which we use for normalizing the continuous correction function  $\varepsilon(\lambda)_{\text{uncorr}}$  obtained from a continuum spectrum.

The emission spectra of NO and  $\text{N}_2$  molecules used for calibration we measured in a double ICP-RF-discharge (13.56 MHz) at 1500 W,  $p = 10 \text{ Pa}$  in a 10/1  $\text{N}_2/\text{O}_2$  mixture and a 10/1  $\text{Ar}/\text{N}_2$  mixture, respectively. In these discharges NO molecules are the product of a surface-recombination process at the stainless steel walls of the discharge chamber



and the volume reaction



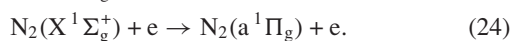
They are excited by electron impact according to the reaction schemes



and by reactions with metastable excited species according to



The  $\text{N}_2$  molecules are excited by the electron impact reactions



See [5]. The plasma is optically thin for all molecular radiations used for calibration.

Due to the high resolution of the ESA 3000 the vibrational structures in the  $\text{N}_2$  emission spectrum (LBH and second positive systems) are well resolved. We integrated the radiation of each vibrational transition over its rotational structure for determining the intensity of the entire transition. In  $\text{N}_2/\text{O}_2$  discharges of low gas pressure NO molecules are mainly excited by reaction (22) and hence into high rotational states. Where the vibrational bands were broad and overlapped we determined the NO vibrational distributions by means of a calculation of the  $\text{NO}(A-X)$  spectra, with the program LIFBASE [6]. The value of the rotational temperature  $T_r$  for each vibrational sequence we obtained by fitting the emission spectra, calculated by LIFBASE, to regions of the measured spectra without overlapping bands using the intensity and  $T_r$  as fit parameters. For the  $\text{NO}(A)$  molecule the rotational temperatures obtained in this way depended on the vibrational quantum number:  $T_r(v' = 0) = 1500 \text{ K}$ ,  $T_r(v' = 2) = 1000 \text{ K}$ . We normalized each band in regions without overlap and integrated the intensity as discussed above.

In optically thin media these emission spectra constitute very reliable relative secondary standards because the intensity distributions in the emission spectra are determined only by the branching ratios of the Einstein coefficients independently of the processes of excitation and depopulation of the excited molecular levels. The intensity distributions in the emission spectra of NO and  $\text{N}_2$  molecules are very well known and documented [5, 7]. Systematic errors of the branching ratios of these vibrational transitions are highly unlikely. We compared the intensity distributions in the measured spectra with the corresponding branching ratios from [8].

For the relative efficiency  $\Phi(\lambda)$  we found no influence of the spectrometer measuring parameters, such as the status of the on-chip-accumulators, the MCP width and the MCP amplification. However,  $\Phi(\lambda)$  changes after revolving the exit of the optical fibre around the fibre-axis. This effect must be taken into account when dismantling the fibre (e.g. in the case of transporting the spectrometer). On average the relative error due to this effect amounts to 6% in the spectral range 400–800 nm and up to 15% around 250 nm. We recommend reconstructing the jacket at the exit of the optical fibre and the respective mounting socket in such a way that the fibre can be mounted only in one well-defined orientation.

#### 4.3. Absolute calibration

To determine the missing factor in  $\varepsilon(\lambda)$  for the absolute calibration of the spectrometer we used the tungsten-ribbon lamp and a spherical mirror. The mirror creates a 1:1 image of the glowing ribbon on the entrance of the ESA 3000 optical fibre. The photon flux through the entrance hole was calculated from the spectral radiance data of the tungsten lamp, the solid angle of the spherical mirror, the reflectivity of the aluminium mirror surface and the cross-section of the entrance hole of the fibre. In this way we determined at some benchmark wavelengths the function  $\varepsilon_{\text{exp}}(\lambda)$  according to the relation

$$\varepsilon_{\text{exp}}(\tilde{\lambda}) \cdot I(X) = d\Psi(\lambda)/d\lambda|_{\tilde{\lambda}} \quad (25)$$

and corrected  $\varepsilon(\lambda)$  accordingly. In this way we achieved for the absolute calibration 12% accuracy.

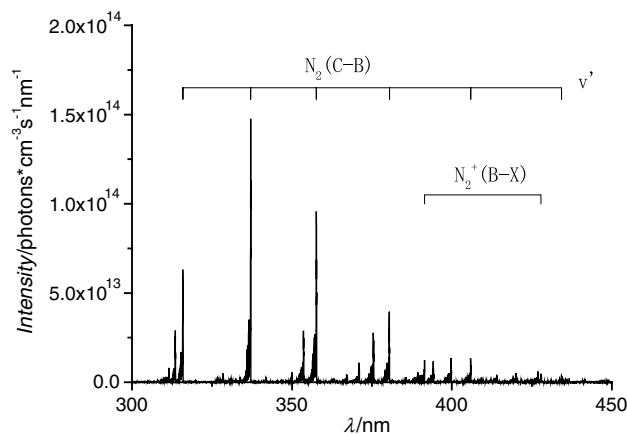


**Figure 10.** Part of a corrected experimental spectrum of an ICP discharge in nitrogen ( $p = 10$  Pa,  $f = 13.56$  MHz,  $P = 1500$  W).

In the case of continuum radiation we obtain by performing the correction

$$\varepsilon_{\text{exp}}(\tilde{\lambda}) \cdot I(X) = \Delta \Psi_{\text{pixel}} / \Delta \lambda_{\text{pixel}} \approx d\Psi(\lambda) / d\lambda|_{\tilde{\lambda}}, \quad (26)$$

which is the desired quantity.

In the case of line radiation we want to determine  $\Psi_{\text{line}}$ , a radiation flux, no spectral density. This can be reached by two different methods demonstrated in the following equation:

$$\Psi_{\text{line}} = \sum_{\text{line}} \varepsilon_{\text{exp}}(\lambda) \cdot I_i \cdot \Delta \lambda_{\text{pixel}} \approx \int_{\text{line}} \varepsilon_{\text{exp}}(\lambda) I d\lambda. \quad (27)$$

After having corrected the spectrum we either multiply the sum of the pixel signals by  $\Delta \lambda_{\text{pixel}}$  or we integrate the pixel signals over the wavelength scale. The integration can be performed numerically without knowing the exact value of  $\Delta \lambda_{\text{pixel}}$ . This is in many cases an advantage. We used the latter method.

## 5. Some typical results from a nitrogen ICP-discharge

To demonstrate the potential of the ESA 3000 spectrometer for plasma diagnostics we report some results from a continuously pumped low pressure ( $p = 10$  Pa) 13.56 MHz ICP-discharge running in nitrogen at about 1500 W absorbed RF power.

Parts of the measured nitrogen spectra are presented in figures 10 and 11. With the spectral resolution of the ESA 3000 we not only resolved the respective electronic and vibrational distributions (figure 10) but also the rotational distributions (figure 11). Above 11 eV electron kinetic energy the electron temperature can be determined by means of the intensity ratios of the  $\text{N}_2(\text{C-B})$  and  $\text{N}_2^+(\text{B-X})$  transitions. In the range  $1.5 \text{ eV} \leq E \leq 4.5 \text{ eV}$  the electron temperature can be determined from the  $\text{N}_2(\text{C-B})$  vibrational band [4, 9]. The average electron density can be evaluated from absolute intensities of measured molecular bands.

Under ICP discharge conditions the rotational distribution of the nitrogen molecules corresponds to the gas temperature despite the low gas pressure [10] and can be determined from the emission spectrum by fitting calculated intensity distributions to measured ones; see figure 11. (Here the influence of the change of the dispersion over the spectral range

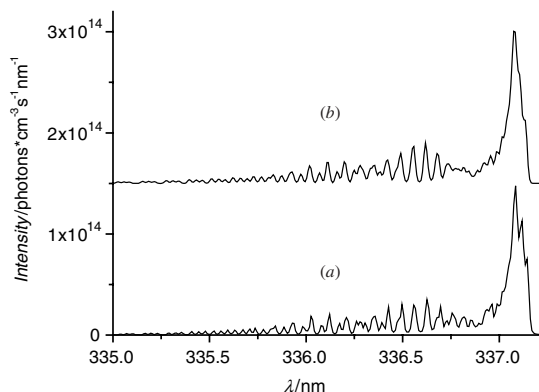


**Figure 11.** Corrected experimental (a) and calculated (b) rotational band of the  $\text{N}_2(\text{C-B}, 0-0)$  emission demonstrating the high resolution of the EAS 3000. The measurement is an enlarged detail of the spectrum displayed in figure 10. For the calculation a rotational temperature  $T_r = 350 \pm 30$  K was used and the zero of the calculated spectrum is shifted to  $1.5 \times 10^{14}$  photon  $\text{cm}^{-3} \text{ s}^{-1} \text{ nm}^{-1}$ .

of a rotational distribution is small and need not be considered as in the case of vibrational spectra.) More detailed results from low-pressure discharges will be given in a subsequent publication.

## 6. Conclusions

We have relatively and absolutely calibrated an echelle spectrometer by means of an adjustable combination of a tungsten-ribbon and a deuterium lamp, using as standard a tungsten ribbon lamp and the branching ratios in the emission spectra of NO and  $\text{N}_2$  molecules. For the example of an ICP nitrogen discharge at 13.56 MHz we demonstrate the advantages of this modern broadband spectrometer for plasma diagnostic. Emission spectra can be measured with spatial and temporal resolution. Due to the short time interval necessary to obtain a total emission spectrum in the very broad range from 200 to 800 nm with high resolution, systematic errors induced by unstable plasma conditions are negligible. The well-resolved rotational structures of molecular emission bands give information on the gas temperature under discharge conditions. The electron distribution function can be determined from the electronic and vibrational intensity distributions of the spectra of two-atom molecules. Special problems are caused by the complicated calibration procedure, the dependence of the efficiency on the dispersion and the spectral regions with zero efficiency.

## Acknowledgments

The authors thank Dr K Löbe, LLA Instruments GmbH, for providing us technical information on the echelle spectrometer ESA 3000 and figure 1. This work was supported by the Deutsche Forschungsgemeinschaft, Bonn-Bad Godesberg under the auspices of SFB 591 ‘Universelles Verhalten gleichgewichtsferner Plasmen: Heizung, Transport und Strukturbildung’ and Graduiertenkolleg 1051 ‘Nichtgleichgewichtsphänomene in Niedertemperaturplasmen: Diagnostik-Modellierung—Anwendungen’.

## References

- [1] ESA 3000 Manual, LLA Instruments GmbH, Berlin
- [2] Bibinov N K, Bolshukhin D O, Kokh D B, Pravilov A M, Vinogradov I P and Wiesemann K 1997 Absolute calibration of the efficiency of a VUV-monochromator/detector system in the range 110–450 nm *Meas. Sci. Technol.* **8** 773–81
- [3] Akopyan M E, Bibinov N K, Kokh D B, Pravilov A M and Stepanov M B 1999 The iodine  $E0_g^+ - B0_u^+$  and  $D0_u^+ - X0_g^+$  transition dipole moment functions *Chem. Phys.* **242** 253–61
- [4] Bibinov N K, Bratsev V F, Kokh D B, Ochkur V I and Wiesemann K 2005 Spectroscopic determination of the cold electron population in very low pressure ECR discharges in  $N_2/He$  mixtures *Plasma Sources Sci. Technol.* **14** 109–28
- [5] Piper L G, Cowless L and Rawlins W T 1986 State-to-state excitation of  $NO(A^2\Sigma^+, v' = 0, 1, 2)$  by  $N_2(A^3\Sigma_u^+, v' = 0, 1, 2)$  *J. Chem. Phys.* **85** 3369–78
- [6] Luque J and Crosley D R 1999 LIFBASE: Database and Spectral Simulation Program (Version 1.5) *SRI International Report* MP 99–009
- [7] Lofthus A and Krupenie P H 1977 The spectrum of molecular nitrogen *J. Phys. Chem. Ref. Data* **6** 113–307
- [8] Laux C O and Kruger C H 1992 Arrays of radiative transition probabilities for the  $N_2$  first and second positive, NO beta and gamma,  $N_2^+$  first negative, and  $O_2$  Schumann–Runge band systems *J. Quant. Spectrosc. Radiat. Transfer* **48** 9–24
- [9] Bibinov N K, Kokh D B, Kolokolov N B, Kostenko V A, Meyer D, Vinogradov I P and Wiesemann K 1998 A comparative study of the electron distribution function in the positive columns in  $N_2$  and  $N_2/He$  dc glow discharges by optical spectroscopy and probes *Plasma Sources Sci. Technol.* **7** 298–309
- [10] Bakowski B, Hancock G, Ritchie G A and Thornton L J 2004 Characterization of an inductively coupled  $N_2$  plasma using sensitive diode laser spectroscopy *J. Phys. D: Appl. Phys.* **37** 2064–72